The Astrophysical Journal, 946:62 (12pp), 2023 April 1 https://doi.org/10.3847/1538-4357/acbea4

First BISTRO Observations of the Dark Cloud Taurus L1495A-B10: The Role of the Magnetic Field in the Earliest Stages of Low-mass Star Formation

Derek Ward-Thompson[1], Janik Karoly[1], Kate Pattle[2], Anthony Whitworth[3], Jason Kirk[1], David Berry[4], Pierre Bastien[5], Tao-Chung Ching[6], Simon Coudé[7,8], Jihye Hwang[9,10], Woojin Kwon[11,12], Archana Soam[13], Jia-Wei Wang[14], Tetsuo Hasegawa[15], Shih-Ping Lai[14,16], Keping Qiu[17,18], Doris Arzoumanian[19], Tyler L. Bourke[20,21], Do-Young Byun[9,10], Huei-Ru Vivien Chen[14,16], Wen Ping Chen[22], Mike Chen[23], Zhiwei Chen[24], Jungyeon Cho[25], Minho Choi[9], Youngwoo Choi[26], Yunhee Choi[9], Antonio Chrysostomou[20], Eun Jung Chung[25], Sophia Dai[27], Victor Debattista[1], James Di Francesco[23,28], Pham Ngoc Diep[29], Yasuo Doi[30], Hao-Yuan Duan[16], Yan Duan[27], Chakali Eswaraiah[31], Lapo Fanciullo[32], Jason Fiege[33], Laura M. Fissel[34], Erica Franzmann[33], Per Friberg[4], Rachel Friesen[35], Gary Fuller[21], Ray Furuya[36], Tim Gledhill[37], Sarah Graves[4], Jane Greaves[3], Matt Griffin[3], Qilao Gu[38], Ilseung Han[9,10], Saeko Hayashi[39], Thiem Hoang[9,10], Martin Houde[40], Charles L. H. Hull[41,42,100], Tsuyoshi Inoue[43], Shu-ichiro Inutsuka[44], Kazunari Iwasaki[45], Il-Gyo Jeong[9,46], Doug Johnstone[23,28], Vera Könyves[1], Ji-hyun Kang[9], Miju Kang[9], Akimasa Kataoka[47], Koji Kawabata[48,49,50], Francisca Kemper[51,52,53], Jongsoo Kim[9,10], Shinyoung Kim[9], Gwanjeong Kim[54], Kyoung Hee Kim[9], Mi-Ryang Kim[55], Kee-Tae Kim[9,10], Hyosung Kim[11], Florian Kirchschlager[56], Masato I. N. Kobayashi[19], Patrick M. Koch[14], Takayoshi Kusune[57], Jungmi Kwon[58], Kevin Lacaille[59,60], Chi-Yan Law[61,62], Chang Won Lee[9,10], Hyeseung Lee[25], Yong-Hee Lee[4,63], Chin-Fei Lee[14], Jeong-Eun Lee[55], Sang-Sung Lee[9,10], Dalei Li[64], Di Li[65], Guangxing Li[66], Hua-bai Li[61], Sheng-Jun Lin[16], Hong-Li Liu[66], Tie Liu[67], Sheng-Yuan Liu[14], Junhao Liu[4], Steven Longmore[68], Xing Lu[38], A-Ran Lyo[9], Steve Mairs[4], Masafumi Matsumura[69], Brenda Matthews[23,28], Gerald Moriarty-Schieven[28], Tetsuya Nagata[70], Fumitaka Nakamura[47,71], Hiroyuki Nakanishi[72], Nguyen Bich Ngoc[29,73], Nagayoshi Ohashi[14], Takashi Onaka[74,75], Geumsook Park[9], Harriet Parsons[4], Nicolas Peretto[3], Felix Priestley[3], Tae-Soo Pyo[39,71], Lei Qian[65], Ramprasad Rao[14], Jonathan Rawlings[2], Mark Rawlings[4,76], Brendan Retter[3], John Richer[77,78], Andrew Rigby[3], Sarah Sadavoy[34], Hiro Saito[79], Giorgio Savini[80], Masumichi Seta[81], Yoshito Shimajiri[82], Hiroko Shinnaga[72], Mehrnoosh Tahani[83], Motohide Tamura[15,58,84], Ya-Wen Tang[14], Xindi Tang[85], Kohji Tomisaka[47], Le Ngoc Tram[86], Yusuke Tsukamoto[72], Serena Viti[87], Hongchi Wang[24], Jintai Wu[17], Jinjin Xie[27], Meng-Zhe Yang[16], Hsi-Wei Yen[14], Hyunju Yoo[25], Jinghua Yuan[27], Hyeong-Sik Yun[88], Tetsuya Zenko[70], Guoyin Zhang[65], Yapeng Zhang[89], Chuan-Peng Zhang[27,65], Jianjun Zhou[64], Lei Zhu[65], Ilse de Looze[87], Philippe André[90], C. Darren Dowell[91], David Eden[92], Stewart Eyres[93], Sam Falle[94], Valentin J. M. Le Gouellec[90,95], Frédérick Poidevin[96,97], Jean-François Robitaille[98], and Sven van Loo[99]

[1] Jeremiah Horrocks Institute, University of Central Lancashire, Preston, PR1 2HE, UK; DWard-Thompson@uclan.ac.uk
[2] Department of Physics and Astronomy, University College London, London, WC1E 6BT, UK
[3] School of Physics and Astronomy, Cardiff University, The Parade, Cardiff, CF24 3AA, UK
[4] East Asian Observatory, 660 N. A'ohōkū Place, University Park, Hilo, HI, 96720, USA
[5] Centre de Recherche en Astrophysique du Québec & Département de Physique, Université de Montréal, C.P. 6128 Succ. Centre-ville, Montréal, QC, H3C 3J7, Canada
[6] Zhejiang Lab, Kechuang Avenue, Yuhang District, Hangzhou 311121, People's Republic of China
[7] Department of Earth, Environment, and Physics, Worcester State University, Worcester, MA 01602, USA
[8] Center for Astrophysics | Harvard & Smithsonian, 60 Garden Street, Cambridge, MA, 02138, USA
[9] Korea Astronomy and Space Science Institute, 776 Daedeokdae-ro, Yuseong-gu, Daejeon 34055, Republic of Korea
[10] University of Science and Technology, Korea, 217 Gajeong-ro, Yuseong-gu, Daejeon 34113, Republic of Korea
[11] Department of Earth Science Education, Seoul National University, 1 Gwanak-ro, Gwanak-gu, Seoul 08826, Republic of Korea
[12] SNU Astronomy Research Center, Seoul National University, 1 Gwanak-ro, Gwanak-gu, Seoul 08826, Republic of Korea
[13] Indian Institute of Astrophysics, II Block, Koramangala, Bengaluru 560034, India
[14] Academia Sinica Institute of Astronomy and Astrophysics, No.1, Sec. 4., Roosevelt Road, Taipei 10617, Taiwan
[15] National Astronomical Observatory of Japan, National Institutes of Natural Sciences, Osawa, Mitaka, Tokyo, 181-8588, Japan
[16] Institute of Astronomy and Department of Physics, National Tsing Hua University, Hsinchu 30013, Taiwan
[17] School of Astronomy and Space Science, Nanjing University, 163 Xianlin Avenue, Nanjing 210023, People's Republic of China
[18] Key Laboratory of Modern Astronomy and Astrophysics (Nanjing University), Ministry of Education, Nanjing 210023, People's Republic of China
[19] Division of Science, National Astronomical Observatory of Japan, 2-21-1 Osawa, Mitaka, Tokyo, 181-8588, Japan
[20] SKA Observatory, Jodrell Bank, Lower Withington, Macclesfield, SK11 9FT, UK
[21] Jodrell Bank Centre for Astrophysics, School of Physics and Astronomy, University of Manchester, Oxford Road, Manchester, UK
[22] Institute of Astronomy, National Central University, Zhongli 32001, Taiwan
[23] Department of Physics and Astronomy, University of Victoria, Victoria, BC V8W 2Y2, Canada
[24] Purple Mountain Observatory, Chinese Academy of Sciences, 2 West Beijing Road, 210008 Nanjing, People's Republic of China
[25] Department of Astronomy and Space Science, Chungnam National University, Daejeon 34134, Republic of Korea
[26] Department of Physics and Astronomy, Seoul National University, Seoul 08826, Republic of Korea
[27] National Astronomical Observatories, Chinese Academy of Sciences, A20 Datun Road, Chaoyang District, Beijing 100012, People's Republic of China
[28] NRC Herzberg Astronomy and Astrophysics, 5071 West Saanich Road, Victoria, BC, V9E 2E7, Canada
[29] Vietnam National Space Center, Vietnam Academy of Science and Technology, Hanoi, Vietnam
[30] Department of Earth Science and Astronomy, Graduate School of Arts and Sciences, The University of Tokyo, 3-8-1 Komaba, Meguro, Tokyo, 153-8902, Japan
[31] Indian Institute of Science Education and Research (IISER) Tirupati, Rami Reddy Nagar, Karakambadi Road, Mangalam (P.O.), Tirupati 517 507, India
[32] National Chung Hsing University, 145 Xingda Rd., South Dist., Taichung City 402, Taiwan
[33] Department of Physics and Astronomy, The University of Manitoba, Winnipeg, Manitoba, R3T2N2, Canada
[34] Department for Physics, Engineering Physics and Astrophysics, Queen's University, Kingston, ON, K7L 3N6, Canada
[35] National Radio Astronomy Observatory, 520 Edgemont Road, Charlottesville, VA, 22903, USA

[36] Institute of Liberal Arts and Sciences Tokushima University, Minami Jousanajima-machi 1-1, Tokushima 770-8502, Japan
[37] School of Physics, Astronomy & Mathematics, University of Hertfordshire, College Lane, Hatfield, Hertfordshire, AL10 9AB, UK
[38] Shanghai Astronomical Observatory, Chinese Academy of Sciences, 80 Nandan Road, Shanghai 200030, People's Republic of China
[39] Subaru Telescope, National Astronomical Observatory of Japan, 650 N. A'ohōkū Place, Hilo, HI, 96720, USA
[40] Department of Physics and Astronomy, The University of Western Ontario, 1151 Richmond Street, London, N6A 3K7, Canada
[41] National Astronomical Observatory of Japan, Alonso de Córdova 3788, Office 61B, Vitacura, Santiago, Chile
[42] Joint ALMA Observatory, Alonso de Córdova 3107, Vitacura, Santiago, Chile
[43] Department of Physics, Konan University, Okamoto 8-9-1, Higashinada-ku, Kobe, 658-8501, Japan
[44] Department of Physics, Graduate School of Science, Nagoya University, Furo-cho, Chikusa-ku, Nagoya, 464-8602, Japan
[45] Department of Environmental Systems Science, Doshisha University, Tatara, Miyakodani 1-3, Kyotanabe, Kyoto, 610-0394, Japan
[46] Department of Astronomy and Atmospheric Sciences, Kyungpook National University, Republic of Korea
[47] Division of Theoretical Astronomy, National Astronomical Observatory of Japan, Mitaka, Tokyo, 181-8588, Japan
[48] Hiroshima Astrophysical Science Center, Hiroshima University, Kagamiyama 1-3-1, Higashi-Hiroshima, Hiroshima, 739-8526, Japan
[49] Department of Physics, Hiroshima University, Kagamiyama 1-3-1, Higashi-Hiroshima, Hiroshima, 739-8526, Japan
[50] Core Research for Energetic Universe, Hiroshima University, Kagamiyama 1-3-1, Higashi-Hiroshima, Hiroshima, 739-8526, Japan
[51] Institute of Space Sciences (ICE), CSIC, Can Magrans, E-08193 Cerdanyola del Vallés, Barcelona, Spain
[52] ICREA, Pg. Lluís Companys 23, Barcelona, Spain
[53] Institut d'Estudis Espacials de Catalunya (IEEC), E-08034 Barcelona, Spain
[54] Nobeyama Radio Observatory, National Astronomical Observatory of Japan, National Institutes of Natural Sciences, Nobeyama, Minamimaki, Minamisaku, Nagano, 384-1305, Japan
[55] School of Space Research, Kyung Hee University, 1732 Deogyeong-daero, Giheung-gu, Yongin-si, Gyeonggi-do 17104, Republic of Korea
[56] Sterrenkundig Observatorium, Ghent University, Krijgslaan 281-S9, B-9000 Gent, BE, Belgium
[57] Astronomical Institute, Graduate School of Science, Tohoku University, Aoba-ku, Sendai, Miyagi, 980-8578, Japan
[58] Department of Astronomy, Graduate School of Science, University of Tokyo, 7-3-1 Hongo, Bunkyo-ku, Tokyo, 113-0033, Japan
[59] Department of Physics and Astronomy, McMaster University, Hamilton, ON, L8S 4M1 Canada
[60] Department of Physics and Atmospheric Science, Dalhousie University, Halifax, B3H 4R2, Canada
[61] Department of Physics, The Chinese University of Hong Kong, Shatin, N.T., Hong Kong
[62] Department of Space, Earth & Environment, Chalmers University of Technology, SE-412 96 Gothenburg, Sweden
[63] School of Space Research, Kyung Hee University, Gyeonggi-do 17104, Republic of Korea
[64] Xinjiang Astronomical Observatory, Chinese Academy of Sciences, Urumqi 830011, Xinjiang, People's Republic of China
[65] CAS Key Laboratory of FAST, National Astronomical Observatories, Chinese Academy of Sciences, People's Republic of China
[66] Department of Astronomy, Yunnan University, Kunming, 650091, People's Republic of China
[67] Key Laboratory for Research in Galaxies and Cosmology, Shanghai Astronomical Observatory, Chinese Academy of Sciences, 80 Nandan Road, Shanghai 200030, People's Republic of China
[68] Astrophysics Research Institute, Liverpool John Moores University, 146 Brownlow Hill, Liverpool, L3 5RF, UK
[69] Faculty of Education & Center for Educational Development and Support, Kagawa University, Saiwai-cho 1-1, Takamatsu, Kagawa, 760-8522, Japan
[70] Department of Astronomy, Graduate School of Science, Kyoto University, Sakyo-ku, Kyoto, 606-8502, Japan
[71] SOKENDAI (The Graduate University for Advanced Studies), Hayama, Kanagawa, 240-0193, Japan
[72] Department of Physics and Astronomy, Graduate School of Science and Engineering, Kagoshima University, 1-21-35 Korimoto, Kagoshima, 890-0065, Japan
[73] Graduate University of Science and Technology, Vietnam Academy of Science and Technology, Hanoi, Vietnam
[74] Department of Physics, Faculty of Science and Engineering, Meisei University, 2-1-1 Hodokubo, Hino, Tokyo, 191-8506, Japan
[75] Department of Astronomy, Graduate School of Science, The University of Tokyo, 7-3-1 Hongo, Bunkyo-ku, Tokyo, 113-0033, Japan
[76] Gemini Observatory/NSF's NOIRLab, 670 N. A'ohōkū Place, Hilo, HI, 96720, USA
[77] Astrophysics Group, Cavendish Laboratory, J.J. Thomson Avenue, Cambridge, CB3 0HE, UK
[78] Kavli Institute for Cosmology, Institute of Astronomy, University of Cambridge, Madingley Road, Cambridge, CB3 0HA, UK
[79] Faculty of Pure and Applied Sciences, University of Tsukuba, 1-1-1 Tennodai, Tsukuba, Ibaraki, 305-8577, Japan
[80] OSL, Physics & Astronomy Dept., University College London, London, WC1E 6BT, UK
[81] Department of Physics, School of Science and Technology, Kwansei Gakuin University, 2-1 Gakuen, Sanda, Hyogo, 669-1337, Japan
[82] Kyushu Kyoritsu University, 1-8, Jiyugaoka, Yahatanishi-ku, Kitakyushu-shi, Fukuoka, 807-8585, Japan
[83] Dominion Radio Astrophysical Observatory, Herzberg Astronomy and Astrophysics Research Centre, National Research Council Canada, P.O. Box 248, Penticton, BC, V2A 6J9 Canada
[84] Astrobiology Center, National Institutes of Natural Sciences, 2-21-1 Osawa, Mitaka, Tokyo, 181-8588, Japan
[85] Xinjiang Astronomical Observatory, Chinese Academy of Sciences, 830011 Urumqi, People's Republic of China
[86] University of Science and Technology of Hanoi, Vietnam Academy of Science and Technology, Hanoi, Vietnam
[87] Physics & Astronomy Dept., University College London, London, WC1E 6BT, UK
[88] Korea Astronomy and Space Science Institute, Yuseong-gu, Daejeon 34055, Republic of Korea
[89] Department of Astronomy, Beijing Normal University, Beijing 100875, People's Republic of China
[90] Laboratoire d'Astrophysique (AIM), Université Paris-Saclay, Université Paris Cité, CEA, CNRS, AIM, F-91191 Gif-sur-Yvette, France
[91] Jet Propulsion Laboratory, M/S 169-506, 4800 Oak Grove Drive, Pasadena, CA, 91109, USA
[92] Armagh Observatory and Planetarium, College Hill, Armagh, BT61 9DG, UK
[93] University of South Wales, Pontypridd, CF37 1DL, UK
[94] Department of Applied Mathematics, University of Leeds, Woodhouse Lane, Leeds, LS2 9JT, UK
[95] SOFIA Science Center, Universities Space Research Association, NASA Ames Research Center, Moffett Field, California, 94035, USA
[96] Instituto de Astrofisíca de Canarias, E-38200 La Laguna, Tenerife, Canary Islands, Spain
[97] Departamento de Astrofísica, Universidad de La Laguna (ULL), E-38206 La Laguna, Tenerife, Spain
[98] Univ. Grenoble Alpes, CNRS, IPAG, F-38000 Grenoble, France
[99] School of Physics and Astronomy, University of Leeds, Woodhouse Lane, Leeds, LS2 9JT, UK
Received 2022 October 10; revised 2023 February 22; accepted 2023 February 22; published 2023 March 30

[100] NAOJ Fellow.

Abstract

We present BISTRO Survey 850 μm dust emission polarization observations of the L1495A-B10 region of the Taurus molecular cloud, taken at the James Clerk Maxwell Telescope (JCMT). We observe a roughly triangular network of dense filaments. We detect nine of the dense starless cores embedded within these filaments in polarization, finding that the plane-of-sky orientation of the core-scale magnetic field lies roughly perpendicular to the filaments in almost all cases. We also find that the large-scale magnetic field orientation measured by Planck is not correlated with any of the core or filament structures, except in the case of the lowest-density core. We propose a scenario for early prestellar evolution that is both an extension to, and consistent with, previous models, introducing an additional evolutionary transitional stage between field-dominated and matter-dominated evolution, observed here for the first time. In this scenario, the cloud collapses first to a sheet-like structure. Uniquely, we appear to be seeing this sheet almost face on. The sheet fragments into filaments, which in turn form cores. However, the material must reach a certain critical density before the evolution changes from being field dominated to being matter dominated. We measure the sheet surface density and the magnetic field strength at that transition for the first time and show consistency with an analytical prediction that had previously gone untested for over 50 yr.

Unified Astronomy Thesaurus concepts: Interstellar magnetic fields (845); Molecular clouds (1072); Starlight polarization (1571); Collapsing clouds (267); Interstellar filaments (842)

1. Introduction

The L1495 region of the Taurus molecular cloud appears as an obscuring dark cloud on optical images (Barnard 1907; Lynds 1962), with a linear, or filamentary, structure, coming to a head at a small globule that is referred to as L1495A (Benson & Myers 1989; Lee et al. 2001), or sometimes as B10 (e.g., Punanova et al. 2018).

Marsh et al. (2016) studied the L1495 filament and found it to be consistent with the filamentary star formation model (André et al. 2014) favored by Herschel observations of star-forming regions (André et al. 2010). Lee et al. (2001) found evidence for asymmetric line profiles in the southern part of L1495A, apparently indicating collapse or contraction. However, this is close to the Herbig Ae/Be star, V892 Tau, which is clearly affecting at least the southern part of L1495A, so interpreting asymmetric line profiles is made more complex in this area.

Ward-Thompson et al. (2016) presented a comparison of SCUBA2 and Herschel observations of the L1495A cloud—see Figure 1. They found that SCUBA2 detects only the highest-surface-brightness sources, principally detecting protostellar sources and starless cores embedded in filaments, while Herschel is sensitive to most of the cloud structure, including extended low-surface-brightness emission. For similar temperature cores, such as those seen in L1495A, the surface brightnesses of the cores are determined by their column densities, with the highest-column-density cores being detected by SCUBA2. For roughly spherical geometries, column density can be related to volume density, and so SCUBA2 selects the densest cores from a population at a given temperature—thus, the cores in Figure 1 appear red. Hence, the polarimeter POL2 on SCUBA2 is most sensitive to the polarization in the cores of L1495A, rather than the filaments.

In this paper we present POL2 data of L1495A as part of the BISTRO survey. In a previous paper from the BISTRO survey (Eswaraiah et al. 2021) we presented data from the B213 part of the L1495 filament, which lies to the southeast of this region. In both cases we concentrate on the polarization of the cores. However, whereas the cores in the previous B213 paper mostly contained YSOs, the cores studied in this paper are all starless.

2. Observations and Data Reduction

2.1. SCUBA2-POL2 Observations

L1495 was observed at 450 and 850 μm, using SCUBA2-POL2 on the James Clerk Maxwell Telescope (JCMT). SCUBA2 only detects Stokes *I*, whereas POL2 also detects *Q* and *U*. Observations were carried out as part of the BISTRO large program between 2020 January and 2021 January (Project ID: M17BL011). Additional observations as part of BISTRO were further carried out between 2021 March and November (Project ID: M20AL018). There were 20 observations completed, each of ≈41 minutes for a total on-source time of ≈14 hr. The observations were carried out in weather bands 1 and 2, which are equivalent to atmospheric opacity at 225 GHz (τ_{225}) ⩽0.05, for the first sets of observations and in the range 0.05–0.08 for the later observations.

The JCMT has a primary dish diameter of 15 m and a beam size of 14.″6 at 850 μm when approximated with a two-component Gaussian (Dempsey et al. 2013). This corresponds to roughly 0.01 pc at a nominal distance to Taurus of 140 pc (Torres et al. 2009; Schlafly et al. 2014; Roccatagliata et al. 2020). The observations were carried out using a SCUBA2 DAISY mode that is optimized for POL2 observations. This produces a central 3′ diameter region with uniform coverage and exposure time. Coverage decreases and noise increases toward the edge of the field of view (Holland et al. 2013). This mode has a scanning speed of 8″ s^{-1} and a half-wave plate with a rotation frequency of 2 Hz (Friberg et al. 2016).

2.2. Data Reduction

The data were reduced using the Submillimetre User Reduction Facility (SMURF) package (Chapin et al. 2013) from the Starlink software (Currie et al. 2014). The SMURF package contains the data reduction routine for SCUBA2-POL2 observations named `pol2map`, which is used for both 450 and 850 μm. In this paper we only consider the 850 μm data.

Initially, the raw bolometer time streams are separated into separate Stokes *I*, *Q*, and *U* time streams. The command *makemap* (Chapin et al. 2013) is then called to create an initial Stokes *I* map from the Stokes *I* time streams. The second step

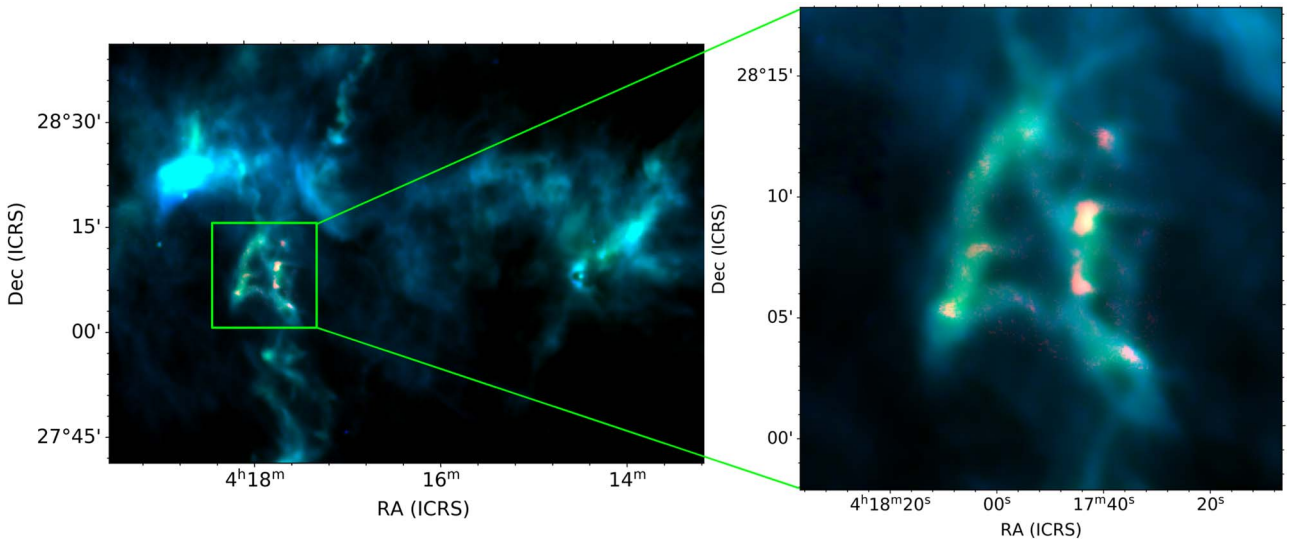

Figure 1. Left: false-color red–green–blue (RGB) image of the L1495A region taken from the SCUBA2 and Herschel-SPIRE observations of Ward-Thompson et al. (2016). Red shows the SCUBA2 850 μm observations and green and blue show the 500 and 250 μm Herschel-SPIRE observations, respectively. This region lies at the head of the L1495 filament, which can be seen heading south from the lower left part of the image. Right: zoomed-in region of the green square on the left, showing the region mapped in this paper. The RGB channels are the same as in the left panel.

of the reduction creates the final Stokes *I, Q,* and *U* maps and a polarization half-vector catalog. Note that we refer to the polarization measurements as half-vectors because they have a 180° ambiguity.

We included the parameters *skyloop* and *mapvar* in our reduction (Chapin et al. 2013). Skyloop allows for each observation to be compared to each other at each iteration, as opposed to the previous map-making method where each individual set of observations would iterate individually and then be coadded at the end. Using skyloop allows us to pick up fainter, more extended emission.

Normally, variances in the map are calculated as linear combinations of the variances of each observation (where variances are calculated by the spread of bolometer signals which fall within the pixel). However when using *mapvar*, variances are calculated by the spread across the individual observations.

The reduction was carried out using a pixel size of 8″. This is a larger pixel size than previous SCUBA2-POL2 reductions, which tend to use a pixel size of 4″. However, with lower flux density starless sources such as those in L1495A, a larger pixel size increases the signal-to-noise ratio (S/N) of the Stokes *I, Q*, and *U* maps.

The 850 μm Stokes *I*, *Q*, and *U* maps were also multiplied by a flux conversion factor (FCF) of 748 Jy beam^{-1} pW^{-1} to convert from pW to Jy beam^{-1} and account for the loss of flux from POL2 inserted into the telescope. This value is the standard 495 Jy beam^{-1} pW^{-1} for reductions using 4″ pixels, multiplied by the standard 1.35 factor from POL2 (Mairs et al. 2021), and then multiplied by a factor of 1.12 to account for the 8″ pixels. This factor was determined from SCUBA2 calibration plots.[101]

To further increase the S/N of our polarization half-vectors, we binned them to a resolution of 12″ as is standard in previous BISTRO work and to match roughly the primary beam size of the JCMT at 850 μm (Dempsey et al. 2013). The polarization half-vectors are also debiased as described by Wardle & Kronberg (1974) to remove statistical bias in regions of low S/N (see Equation (1)).

The values for the debiased degree of polarization P were calculated from

$$P = \frac{1}{I}\sqrt{Q^2 + U^2 - \frac{1}{2}(\delta Q^2 + \delta U^2)}, \quad (1)$$

where I, Q, and U are the Stokes parameters, and δQ and δU are the uncertainties in Stokes Q and U . The uncertainty δP of the degree of polarization was obtained using

$$\delta P = \sqrt{\frac{(Q^2\delta Q^2 + U^2\delta U^2)}{I^2(Q^2 + U^2)} + I\frac{\delta I^2(Q^2 + U^2)}{I^4}}, \quad (2)$$

with δI being the uncertainty in Stokes I (total intensity).

The polarization position angles θ, measured from north through east on the plane of the sky, were calculated using the relation

$$\theta = \frac{1}{2}\tan^{-1}\frac{U}{Q}. \quad (3)$$

The corresponding uncertainties in θ were calculated using

$$\delta\theta = \frac{1}{2}\frac{\sqrt{Q^2\delta U^2 + U^2\delta Q^2}}{(Q^2 + U^2)} \times \frac{180^\circ}{\pi}. \quad (4)$$

We chose S/N cuts of $I/\delta I > 10$ and $P/\delta P > 2$, as is standard for making SCUBA2-POL2 polarization maps. This corresponded to a minimum flux density of around 10 mJy beam^{-1}. The number of individual positions at which we detect polarization at this level varies in each core from a couple up to 20 or more. Typically, all of the half-vectors in each core were seen to be lying roughly parallel to each other, so we subsequently averaged the measured polarization half-vectors as a weighted mean (weighted according to their S/N), averaged over the FWHM size of each core (see Table 1), to make a single polarization measurement of each core.

[101] https://www.eaobservatory.org/jcmt/instrumentation/continuum/SCUBA2/calibration

Table 1
Core Characteristics

Core No.[a]	R.A. (J2000)	Decl. (J2000)	FWHM[b] ($'' \times ''$)	θ_{core}[b,c] (°)	θ_{fil}[c,d] (°)	Temp.[b] (K)	$N(H_2)$[e] ($\times 10^{21}$ cm^{-2})	$n(H_2)$ ($\times 10^5$ cm^{-3})	A_V[f] (mag)	θ_{pol}[c] (°)
1 (2)	4:17:42.10	+28:08:44.4	54.6 × 21.4	167	26	10.1 ± 0.2	19.1 ± 7.6	2.0 ± 0.8	17 ± 7	4 ± 2
2-N (7)	4:17:43.75	+28:07:04.6	32.0 × 16.0	0	0	10.6 ± 0.2	14.7 ± 5.9	2.4 ± 1.0	13 ± 5	−3 ± 4
2-S (7)	4:17:43.40	+28:06:04.5	32.4 × 20.7	45	0	10.6 ± 0.2	15.7 ± 6.3	2.1 ± 0.8	14 ± 6	−46 ± 3
3 (12)	4:17:34.58	+28:03:05.0	55.2 × 20.3	53	37	12.7 ± 0.3	15.3 ± 6.1	1.6 ± 0.6	14 ± 6	68 ± 11
4 (−)	4:17:53.92	+28:05:28.3	31.4 × 12.1	60	85	12.5 ± 0.1	9.2 ± 3.7	1.7 ± 0.7	8 ± 3	−72 ± 8
5 (5)	4:18:08.17	+28:05:10.3	39.6 × 32.0	121	150	10.1 ± 0.2	17.8 ± 7.1	1.8 ± 0.7	16 ± 7	−4 ± 12
6 (11)	4:18:03.08	+28:07:35.2	39.0 × 20.5	126	170	9.3 ± 0.2	14.0 ± 5.6	1.8 ± 0.7	13 ± 5	18 ± 5
7 (19)	4:18:00.55	+28:11:08.7	45.0 × 22.2	165	147	10.7 ± 0.2	14.4 ± 5.8	1.7 ± 0.7	13 ± 5	9 ± 6
8 (14)	4:17:52.08	+28:12:31.1	51.6 × 48.7	93	135 (15)	10.9 ± 0.2	14.1 ± 5.6	1.0 ± 0.4	13 ± 5	−13 ± 7

Notes.
[a] Core number in parentheses from Ward-Thompson et al. (2016).
[b] Values taken from Ward-Thompson et al. (2016).
[c] All angle values are measured east of north.
[d] We adopt ±10° for the local filament angle except in cores 4 and 8 (see Section 3.2).
[e] Column density values from the Gould Belt Survey (Palmeirim et al. 2013).
[f] A_V calculated using $N_H/A_V \sim 2.2 \times 10^{21}$ cm^{-2} mag^{-1} (Güver & Özel 2009) and $N(H_2) \sim 0.5\, N_H$.

The plane-of-sky orientation of the magnetic field is inferred by rotating the polarization angles by 90°, assuming that the polarization is caused by elongated dust grains aligned perpendicular to the magnetic field (see Andersson et al. 2015 and references therein). This is true for dust grains in the Rayleigh regime (Kirchschlager et al. 2019; Guillet et al. 2020), and for observations at 850 μm this is fulfilled for dust grains with sizes up to roughly 100 μm, which form the majority of those we observe. This single measurement of the *B*-field is what is plotted at the position of each core in Figure 2 and listed in Table 1.

3. Results

3.1. Cores

Figure 1 (left) shows a false-color image (adapted from Ward-Thompson et al. 2016), in which green and blue are taken from the Herschel-SPIRE images of the region at 500 and 250 μm, respectively, and red is the SCUBA2 850 μm Stokes *I* emission. The much larger-scale B211-213 L1495 filament (e.g., Marsh et al. 2016) can be seen beginning at the southern edge of this field and extending southwards out of the field of view. Figure 1 (right) shows a close up of the triangle of filamentary structures observed by Ward-Thompson et al. (2016). This is the region observed by BISTRO. The dense cores show up clearly in the 850 μm data as red sources, as mentioned above. These are all starless cores and candidate prestellar cores (Ward-Thompson et al. 2016; Howard et al. 2019).

We here assign the cores numbers as shown in Figure 2, which has the same background as Figure 1 (right). One core where we have detected polarization was not identified as a core by Ward-Thompson et al. (2016), as it was only detected very faintly in the earlier work. This is labeled in Figure 2 as core 4. Hence, if we include core 4 among the list of cores detected earlier, we find that we only detect polarization at this level at the cores themselves. We also note that core 2 appears to be split into two cores in the Stokes *I* image, which we here label 2N and 2S. Core 2 was not identified as a double core by Ward-Thompson et al. (2016). The two cores 2N and 2S have

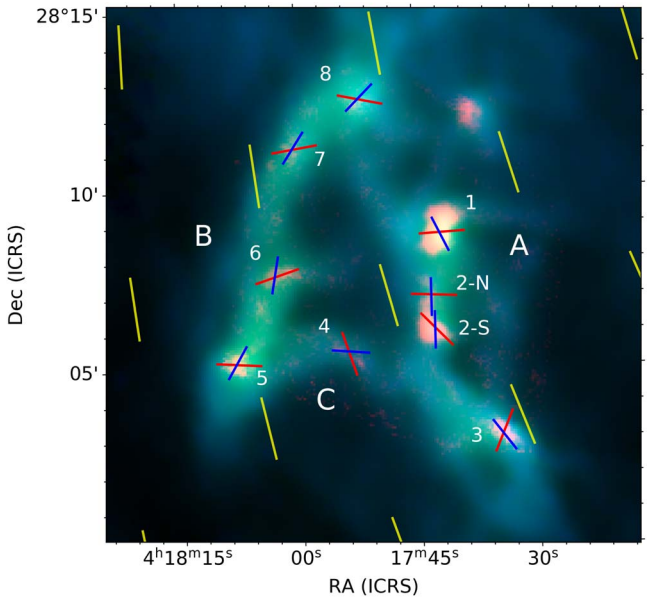

Figure 2. Same background image as in Figure 1. The filaments seen in the original SCUBA2 and Herschel images are clearly seen and are labeled "A," "B," and "C," as described in the text. The cores that we identify in this paper are numbered 1 to 8 as described in the text. Superposed on this image are rotated polarization half-vectors to demonstrate the orientation of the magnetic field. The red vectors show the mean magnetic field orientation in each core from the POL2 observations. The yellow vectors show the orientation of the large-scale magnetic field (oversampled) from Planck observations (there are only about four independent Planck beams in this whole field of view). The blue half-vectors show the local filament major axis orientation (for core 8 we only show the axis of filament B). Each set of vectors in this image has a constant length for clarity.

very different polarization orientations. We therefore have a sample of nine cores.

Table 1 lists the cores detected in L1495A here in our BISTRO POL2 survey. We also state the core numbers assigned to them by Ward-Thompson et al. (2016), who fitted elliptical Gaussians to each of the cores, and we list the properties of those ellipses also in Table 1 (recall that 30″ is roughly 0.02 pc at a nominal distance of 140 pc to Taurus). We note that core 21 from Ward-Thompson et al. (2016) is in our

field of view, but no detectable polarized emission was observed at this position. For cores 2N, 2S, and 4 we calculated the parameters of the elliptical Gaussians here.

Table 1 also lists the orientation of the local filament major axis at the position of each core, which we measure here from Figure 2, and the core major axis orientations. Core 8 has two filament angles listed, because it sits at the junction of two filaments. The value that is in brackets is for the western filament (see also below).

Table 1 further lists the chief core parameters of temperature as measured by Ward-Thompson et al. (2016) and the column density which was calculated by Palmeirim et al. (2013) using the Herschel bands at the resolution of SPIRE 250 μm. We calculate the volume number density in Table 1 using the column density values and the 850 μm core sizes from Ward-Thompson et al. (2016). The optical extinction values from Table 1 are calculated using the column density values. We also list the weighted mean of the polarization position angle in each core from this work measured north through east.

Figure 2 shows the SCUBA2-POL2 polarization half-vectors overlaid in red, rotated by 90° to indicate the orientation of the plane-of-sky magnetic field, within each dense core. As explained above, we refer to them as half-vectors because they have a 180° ambiguity (i.e., we do not know which end of the *B*-field half-vectors to put the arrow on). Each half-vector represents the weighted mean polarization angle measured for each core, respectively rotated by 90°.

All half-vectors are shown at the same length for clarity. Also shown on Figure 2 in yellow are the half-vectors of the Planck measurements (oversampled), also rotated by 90° to indicate the large-scale plane-of-sky magnetic field orientation. Additionally, the blue vectors in each core indicate the local filament major axis as listed in Table 1.

3.2. Fields and Filaments

Examination of Figure 2 shows a number of interesting features. The filaments form a roughly triangular pattern on the sky. We here label the western filament "Filament A," the eastern filament "Filament B," and the southern filament that runs roughly east–west "Filament C." Cores 1, 2, and 3 lie in Filament A, with cores 5, 6, and 7 in Filament B. Core 4 lies in Filament C. Core 8 lies at the northern apex of the triangle where Filaments A and B meet.

Figure 2 shows that the magnetic field in cores 1, 2N, and 3 lies roughly orthogonal to the local filament (Filament A) long axis. In core 2S the magnetic field is not orthogonal, but at this point the filament turns through 90°, so it is difficult to define a filament orientation uniquely Core 4 has a magnetic field orientation roughly orthogonal to the western half of Filament C, which turns somewhat at the position of core 4. The magnetic field orientations in cores 5, 6, and 7 also lie roughly orthogonal to their local filament (Filament B) major axis orientation. Core 7 is slightly further from orthogonal than the other two, although we note that here also the local filament orientation turns slightly. The magnetic field of core 8 is roughly orthogonal to filament B.

Figure 3 shows a plot of the core magnetic field orientation for each core on the *y*-axis versus 90° minus its local filament major axis angle on the *x*-axis, in order to quantify the above discussion. Any angle that lay between 180° and 360° has had 180° subtracted from it and any angle that lay between 0° and −180° has had 180° added to it, due to the fact that both the magnetic field orientation and the filament orientation are half-vectors, as discussed above. The exception to this was core 4, whose error bar overlaps the origin, so we extend the plot to slightly negative numbers to accommodate core 4.

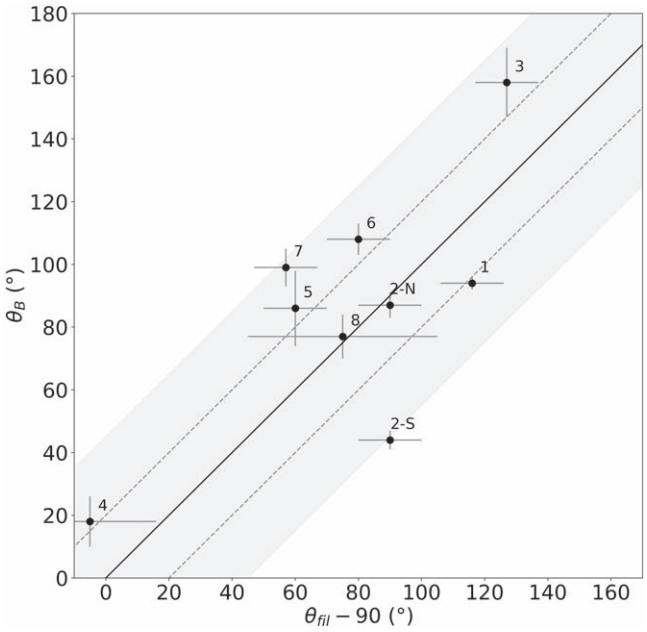

Figure 3. A plot of the core magnetic field orientation for each core on the *y*-axis vs. 90° minus its local filament major axis angle on the *x*-axis. The cores are numbered as in Figure 2. The solid line indicates a one-to-one correlation, which is where the points would be located if the *B*-field lay exactly orthogonal to the local filament orientation in every case. The two dashed lines represent ±20°, roughly matching our predicted systematic angle error at our chosen S/N cut-off. The shaded area is ±45°. See the text for details.

We took the error bar of the filament orientation to be ± 10° as an indication of how accurately we could measure this orientation. For core 4 where the filament is curving we took the filament orientation to be the tangent to the curve and the error bar to be the amount of curvature. For core 8, which lies at the junction of two filaments we took the local filament orientation to be that of filament B, which is denser. The error bar used in the *B*-field orientation in each case is the standard deviation of the angles of the weighted mean half-vectors shown in Figure 2 and listed in Table 1.

If all *B*-field orientations lay exactly orthogonal to their respective filaments, then this plot would show a one-to-one correlation. This is shown by the solid line on Figure 3. We also plot two dashed lines, at +20° and −20° from orthogonal. This is the typical systematic error that we would expect for a 2σ detection of polarization (Naghizadeh-Khouei & Clarke 1993), the value we chose for our cut, as described above. The shaded area represents ±45°.

It can be seen that there is a good degree of correlation in this plot, with most of the points consistent (including error bars) with lying between, or very close to, the dashed lines, and all lying within the shaded area. Hence we conclude that the magnetic fields that we have measured in these cores generally tend to lie closer to orthogonal than parallel to the local filament orientation in which the core is embedded. The core that lies furthest from the correlation line is 2S. This is one of the most dense cores and may have been affected by the proximity of core 2N or the effect of the filament changing orientation from the south to the north of core 2S.

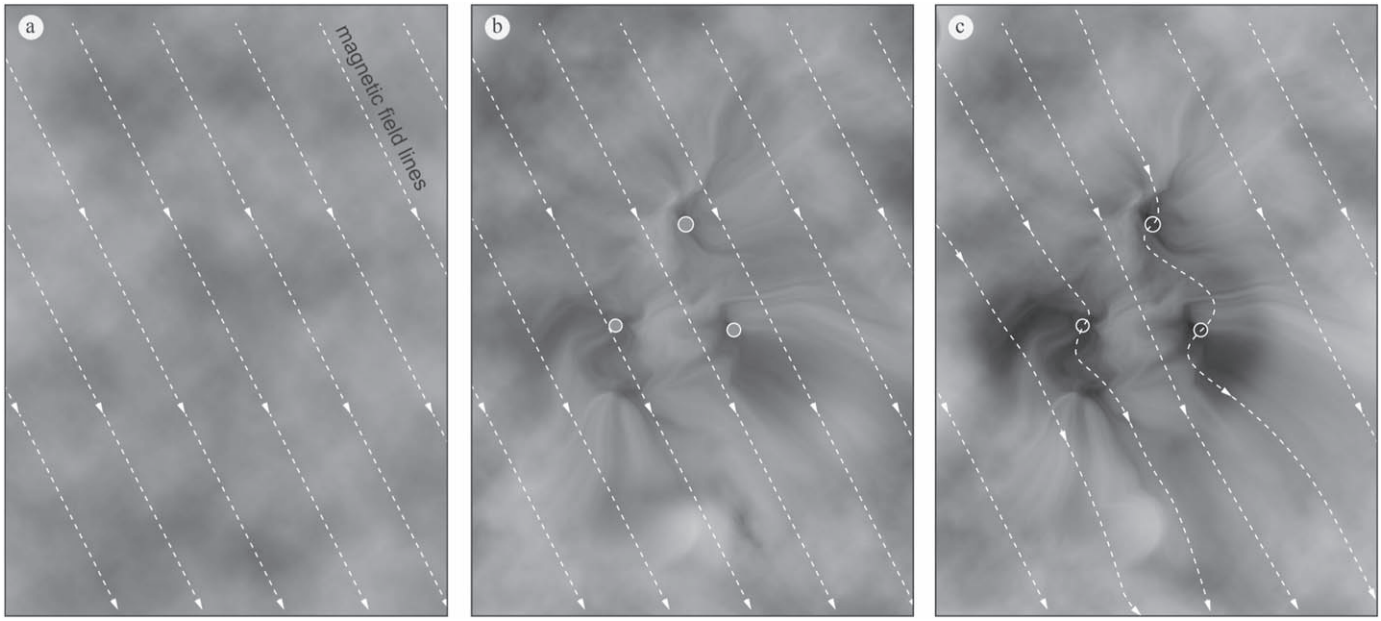

Figure 4. Artist's impression of the three stages of evolution of the filaments and cores in L1495A-B10. The grayscale represents the observer's view of the column density, as seen in Figure 2. The dashed lines with arrows represent the magnetic field and the circles represent the positions of cores. The magnetic field lies initially mostly along the line of sight, with only a small component in the plane of the sky. (a) The magnetically dominated phase: the initial cloud is threaded by a large-scale, uniform magnetic field, largely along the line of sight, as the matter forms a sheet in the plane of the sky. (b) The intermediate phase: the sheet starts to fragment and form filaments, in which low-mass core formation starts. (c) The matter-dominated phase: once the matter of the fragmenting structures crosses a critical surface density, the evolution becomes matter dominated and the subsequent evolution of the matter affects the magnetic field to the extent that the local field is turned to lie perpendicular to the long axis of the local filament orientation at the position of each core.

A similar plot to Figure 3 looking for a correlation between *B*-field orientation and core major axis shows no correlation whatsoever. Likewise a plot of our measured small-scale *B*-field position angles shows no correlation with the large-scale *B*-field orientation measured by Planck, as shown in Figure 2. It can be seen that the local field that we have measured in the starless cores within the filaments has totally dissociated from the large-scale field orientation seen by Planck, and there is no correlation between them.

The exception to this is core 4, whose small-scale *B*-field that we have measured lies almost exactly parallel to the large-scale *B*-field orientation measured by Planck—see Figure 2. This may be a coincidence, because the *B*-field in core 4 also lies roughly perpendicular to its host filament. However, we note that core 4 and the filament in which it sits have the lowest column densities of any of our cores by a factor of 1.5–2 (see Table 1), calculated using standard conversion factors (Güver & Özel 2009; Marsh et al. 2016). Thus it may be the youngest core.

4. Discussion: An Evolutionary Scenario

All of the foregoing leads us to propose an evolutionary scenario for this cloud that is illustrated graphically in Figure 4. This is an artist's impression of the three stages of evolution of the filaments and cores in L1495A-B10. The grayscale represents the observer's view of the column density, as seen in Figure 2. The dashed lines with arrows represent the magnetic field and the circles represent the positions of cores.

We split this evolution into three distinct phases, illustrated by the three panels in Figure 4. We label these phases the magnetically dominated phase (4a), the intermediate phase (4b), and the matter-dominated phase (4c). Figure 4 is an attempt to reproduce the image seen in Figure 2 at different times during this cloud's evolution.

4.1. The Magnetically Dominated Phase

This phase is illustrated in Figure 4(a) and is predicted by theory to be the earliest phase of evolution from an interstellar cloud to the formation of a star. Flux freezing in this phase predicts that the magnetic field should have a significant effect on any structure that is formed. This phase is also commonly referred to as being magnetically subcritical (Crutcher 2004).

Hence we hypothesize a scenario to explain why, in our observations herein of L1495A-B10 on the plane of the sky, the filament orientations appear totally unrelated to one another and to the orientation of the large-scale Planck field. We hypothesize that the *B*-field lies mostly along the line-of-sight orientation, with a small component in the plane of sky. Note that this can be explained, because, for a small range of viewing orientations around the *B*-field axis, there will be both a clearly visible filament, and a significant component of the field apparently approximately perpendicular to the filament.

If the large-scale field does indeed lie close to the line of sight to the cloud, then the percentage polarization seen in the Planck data would be lower at this point than elsewhere in Taurus. We looked at the Planck data (Planck XIX) and found that this is in fact is the case. L1495A-B10 does indeed lie in a "polarization hole" (a minimum of percentage polarization) relative to other nearby regions of Taurus. Hence, our hypothesis to explain our data is also consistent with the Planck data, although this does not constitute proof, since polarization holes can also be caused by other mechanisms.

In this magnetically dominated phase, the material moves mostly along the line of sight, parallel to the *B*-field, both toward and away from the observer (see Figure 4(a)). These

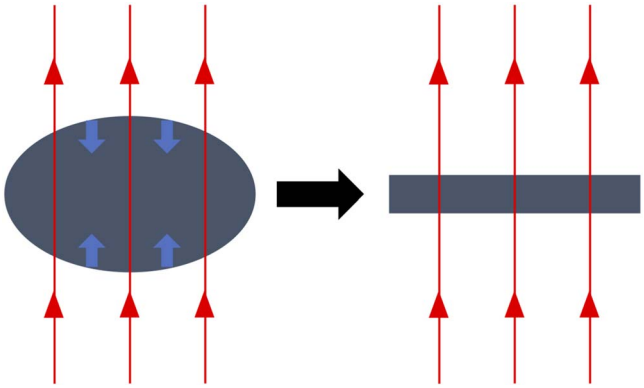

Figure 5. Cartoon illustrating the view roughly orthogonal to the plane-of-sky views in Figures 2 and 4. Here the magnetic field (red arrows) is orthogonal to the viewing angle. The blue arrows are indicating the direction the matter is flowing. The observer is either looking upwards from the bottom of this image or downwards from the top. The transition from left to right is indicating the evolution occurring during the phase illustrated in Figure 4(a), but here seen edge on. See the text for discussion.

counterflows toward and away from us, that feed matter into a denser layer, are assumed to be oblique, and therefore produce a mildly sheared layer, as one would expect for the general case. Since we are assuming ideal MHD the flow is mostly aligned with the magnetic field (the path of least resistance). Any motion of the matter perpendicular to the field lines has to drag the field with it. Consequently, the material that we see lies mostly in a sheet-like structure close to the plane of the sky —i.e., we are seeing the sheet almost face on.

We illustrate the evolution occurring during this phase in Figure 5. This cartoon illustrates the view roughly orthogonal to the plane-of-sky views in Figures 2 and 4. Here the magnetic field (in red) is orthogonal to the viewing angle. The observer is either looking upwards from the bottom of this image or downwards from the top.

On the left of Figure 5 we see the initial cloud threaded by a magnetic field. The blue arrows on the cloud edges indicate the principal directions of collapse along the magnetic field orientation. On the right we see the cloud at the end of the magnetically dominated phase. The cloud has now collapsed to a sheet-like structure, here seen edge on, orthogonal to the orientation of the magnetic field.

4.2. The Intermediate Phase

Once the structures are sufficiently dense to cross a certain critical surface density threshold, the gas motions of the cloud start to transition from magnetically dominated to matter dominated. The sheet fragments under self-gravity and filaments form in a fairly complex web-like manner, all orthogonal to the large-scale magnetic field (see Figure 4b). The convergent velocity field producing each filament (i.e., an approximately linear overdensity within the layer) requires a kink in the magnetic field, so that material can slide down the field lines into the filament.

Simulations suggest that the transition to matter-dominated dynamics is associated with a transition from the magnetic field being preferentially parallel to density structures at low column densities to preferentially perpendicular at high column densities (Soler et al. 2013). This transition appears to require converging, likely super-Alfvénic, gas flows (Soler & Hennebelle 2017), and is likely associated with, and potentially a signature of, the transition of the region to gravitational instability (Chen et al. 2016). Although the precise mechanism by which (and gas density at which) this transition occurs varies between models (see, e.g., Pattle et al. 2022a for a recent review), a large-scale magnetic field strong enough to impose a preferred gas flow direction parallel to the field at low densities is typically required (Soler & Hennebelle 2017).

Figure 4(b) is intended to show the cloud in the process of crossing from the magnetically dominated phase to the matter-dominated phase. Clearly, this change is not instantaneous and takes a finite length of time. The period of the transition is what we here refer to as the intermediate phase seen in Figure 4(b). We here hypothesize that core 4 may still be in this phase, with its magnetic field orientation still parallel to that of the initial large-scale field.

4.3. The Matter-dominated Phase

We would expect the filaments starting to form low-density cores would cause a realignment of the magnetic field orientations within them (see the change from Figures 4(b) to (c)). This phase is sometimes referred to as being magnetically supercritical (Crutcher 2004), or matter dominated (our chosen term).

This is now the scenario depicted in Figure 4(c), which is intended to show the picture largely seen in the observations across the majority of Figure 2.

Thus we see that the filaments influence the local small-scale magnetic field orientation, turning it to tend to lie apparently roughly orthogonal to the long axis of the local filament (see Figure 4(c)). Thereafter, the filaments start to form low-density cores. All cores in L1495A-B10 other than core 4 are here hypothesized to be in this phase.

The cores and filaments then start to increase in density due to accretion of surrounding material. However, the cores are still at an early stage in the star-forming process, since none of them contains a compact protostellar object yet (Ward-Thompson et al. 2016). Similarly, the filaments are probably also in a fairly early stage of development. This is a slight variation on a picture that has previously been proposed—e.g., André et al. (2014) and Seo et al. (2019)—in that it adds an extra transitional evolutionary phase to the picture that we have here observed for the first time.

Simulations suggest that a transition in magnetic field orientation within molecular clouds from lying parallel to perpendicular to density structure occurs only in the case where magnetic fields are dynamically important on large scales (e.g., Soler et al. 2013; Seifried et al. 2020). Planck Collaboration et al. (2016) find a significantly subcritical mass-to-flux ratio of ~0.2–0.4 on large scales in Taurus, while Soler (2019) find from Planck observations that in the L1495/B213 filament (just to the south of the region studied here), a transition from preferentially parallel to preferentially perpendicular occurs at $N_{\rm H} \sim 10^{21.5}\,{\rm cm}^{-2}$. The balance of evidence suggests that the cloud is still magnetically dominated on large scales.

Note that our scenario for the evolution of L1495A-B10 is consistent with BISTRO observations of other nearby filaments with embedded starless cores (except that the field is not along the line of sight), including Perseus NGC 1333 (Doi et al. 2020), Ophiuchus L1689 (Pattle et al. 2021), and Serpens Main (Kwon et al. 2022). All of these clouds have magnetic field orientations consistent with being perpendicular to the local

filament orientation, and apparently agnostic to the large-scale magnetic field orientation in the region.

4.4. Comparison with Theory

The magnetically to matter-dominated transition critical volume density is not well defined. Different theoretical simulations produce transitions at volume number densities in the range 10^2–$10^6\,\mathrm{cm}^{-3}$, with no apparent dependence on Alfvén Mach number (Pattle et al. 2022a). We thus need observational constraints on the transition critical surface density in a range of environments.

However, calculations of the critical column density at which this transition occurs date back over 50 yr (e.g., Mestel 1965—see his Equation (85)), in which a relatively idealized case of a uniform magnetic field threads a uniform density cloud (see also Equation (4.82) in Ward-Thompson & Whitworth 2011). Figure 5 shows a simplified cartoon of the picture we are hypothesizing of a cloud collapsing to a sheet, followed by the fragmentation of the sheet to form filaments and cores (Figure 4) above a certain sheet critical surface density, which we are referring to as the surface density of the transition from the magnetically to the matter-dominated phase.

The above-cited equations lead to a prediction of the relation between the critical surface density, Σ_c, and the magnetic field strength, B, at which the transition occurs, of the form

$$\Sigma_c = (5/G)^{1/2}\,(B/3\pi), \tag{5}$$

which yields

$$[N(\mathrm{H_2})/\mathrm{cm}^{-2}] \simeq 2 \times 10^{20} \times [B/\mu G]. \tag{6}$$

This equation contains uncertainties of a small numerical factor of order unity (e.g., Nakano & Nakamura 1978), but is nevertheless a useful theoretical order-of-magnitude prediction.

Our hypothesized scenario outlined in Sections 4.1–4.3 above, together with our interpretation of the data in Section 3.2 that core 4 may be the youngest core and still undergoing the change from the magnetically to the matter-dominated phase, would lead us to set the critical column density $N(H_2)$ at around $9.2 \times 10^{21}\,\mathrm{cm}^{-2}$. Inserting this value into Equation (6) above predicts an order-of-magnitude magnetic field strength in L1495A-B10 of $\sim$46 μG. If core 4 has passed the critical point of the intermediate phase, then this B-field value is an upper limit.

This compares to a literature value of 25–77 μG from optical and near-infrared observations (Chapman et al. 2011) for L1495A-B10. The equivalent Planck value is 13–32 μG (Planck Collaboration et al. 2016) for the large-scale field around the Taurus region as a whole.

We performed an approximate Davis–Chandrasekhar–Fermi (DCF; Davis 1951; Chandrasekhar & Fermi 1953) analysis in core 1, where we have sufficient half-vectors to make this statistical analysis. For this DCF analysis (e.g., Pattle et al. 2021), we used $\Delta V_{\mathrm{NT}} = 0.206\,\mathrm{km\,s}^{-1}$, which is found from NH_3 velocity dispersion observations (Seo et al. 2015) and then removed the thermal component assuming a temperature of $\sim$10 K. We calculated a dispersion in the magnetic field position angle of $11\overset{\circ}{.}8$ and used the $n(H_2)$ value of core 1 from Table 1. We obtained an upper limit of $\approx$70 μG.

To summarize all of the above: we have hypothesized that L1495A-B10 is evolving from the magnetically dominated phase to the matter-dominated phase, as the face-on sheet that we are observing starts to fragment into filaments and cores. We have further hypothesized that our observed core 4 may be exactly in that transition phase. We have used theoretical arguments to predict what field strength would correspond to this transition at the column densities we observe. Our theoretical prediction for the field strength required is $\sim$46 μG. We have estimated the field strength and, along with literature values, found a range of observed field strengths of 13–32, 25–77, and $\leqslant$70 μG. Hence we see that the whole picture is mutually self-consistent. The theory predicts a B-field strength that is right in the range of measured values.

Hence the theoretical prediction of Mestel (1965) is consistent with our observations, and we have managed to test this prediction fully for the first time in over 50 yr.

4.5. Subsequent Evolution

Using the ratio $N_{\mathrm{H}}/A_V \sim 2.2 \times 10^{21}\,\mathrm{cm}^{-2}\,\mathrm{mag}^{-1}$ (Güver & Özel 2009), the corresponding value of A_V for core 4 at the column density discussed above is $A_V \sim 8$ (assuming $N(H_2) \sim 0.5\,N_{\mathrm{H}}$). This is consistent with the star formation threshold at which molecular clouds can begin to form stars at $A_V \sim 7$–8, discussed by, e.g., Johnstone et al. (2004), Könyves et al. (2015), Marsh et al. (2016), among others, and with the observations collated by Soler (2019), given that it has not yet begun to form stars.

The subsequent behavior of magnetic fields in regions with embedded young stellar objects (YSOs) appears to be more complex. Notably, in Taurus B213, a more-evolved region located elsewhere in the filament of which L1495A-B10 forms the head, the average magnetic field orientation within the embedded dense cores varies significantly, with no clear correlation with either filament or outflow orientation (Eswaraiah et al. 2021). More generally, YSO outflows appear to have the potential to reshape magnetic fields in their vicinities (e.g., Lyo et al. 2021; Yen et al. 2021; Pattle et al. 2022b), suggesting that we cannot infer the magnetic initial conditions for star formation in environments with embedded YSOs.

Therefore, as a region without embedded YSOs, L1495A-B10 represents a more pristine environment in which to study the behavior of magnetic fields in the early stages of filament fragmentation and core formation.

5. Summary

In this paper we have presented the first polarization data from BISTRO of the dark cloud L1495A-B10 in the Taurus molecular cloud, at a wavelength of 850 μm. The cloud contains a complex pattern of small-scale filaments, in a roughly triangular morphology, surrounded by a web of lower-density filaments. The main filaments contain cores of varying densities. We detect polarization from nine of the cores, all of which have previously been shown to be starless.

We calculate the mean plane-of-sky orientation of the small-scale magnetic field in each of the cores and compare this to the large-scale field orientation measured by Planck and to the orientation of the filaments and long axes of the cores. There is no correlation between our measurements and those of Planck other than in the lowest-density case, core 4, as expected for the 'youngest' core. There is also no correlation at all with the core orientation.

However, we find a correlation between our small-scale field measurements and filament orientation, in which the field tends

to lie orthogonal to the long axes of the filaments in all cases except for a core that lies near to a bend in its local filament.

We hypothesize a scenario to explain our data, which is an extension of the previous magnetic filamentary model, adding an additional transitional evolutionary phase to the model, which we here observe for the first time. We suggest we are seeing a cloud which was originally magnetically dominated in the process of transition to being matter dominated in its denser regions, with core 4 defining the transition point, since the local field in core 4 is still aligned with the large-scale field, whereas in the others it tends more toward lying orthogonal to the local filament.

We measure the sheet surface density and the magnetic field strength of that transitional phase for the first time and show consistency with the original analytical prediction that has gone untested for over 50 yr (Mestel 1965).

D.W.T. acknowledges funding support from the UK STFC through grant number ST/R000786/1. J.K. acknowledges funding from the Moses Holden Scholarship for his PhD. K.P. is a Royal Society University Research Fellow, supported by grant number URF\R1\211322 The JCMT is operated by the East Asian Observatory on behalf of National Astronomical Observatory of Japan; the UK STFC under the auspices of grant number ST/N005856/1; Academia Sinica Institute of Astronomy and Astrophysics; the Korea Astronomy and Space Science Institute; the Operation, Maintenance and Upgrading Fund for Astronomical Telescopes and Facility Instruments, budgeted from the Ministry of Finance of China. SCUBA2 and POL2 were built through grants from the Canada Foundation for Innovation. This research used the facilities of the Canadian Astronomy Data Centre operated by the National Research Council of Canada with the support of the Canadian Space Agency. The data taken in this paper were observed under the project code M20AL018. The Starlink software (Currie et al. 2014) is currently supported by the East Asian Observatory. The authors wish to recognize and acknowledge the very significant cultural role and reverence that the summit of Maunakea has always had within the indigenous Hawaiian community. We are most fortunate to have the opportunity to conduct observations from this mountain. M.T. is supported by JSPS KAKENHI grant Nos.18H05442, 15H02063, and 22000005. J.K. is supported by JSPS KAKENHI grant No.19K14775. F.P. acknowledges support from the Spanish State Research Agency (AEI) under grant number PID2019-105552RB-C43. F.K. is supported by the Spanish program Unidad de Excelencia María de Maeztu CEX2020-001058-M, financed by MCIN/AEI/10.13039/501100011033. C.E. acknowledges the financial support from grant RJF/2020/000071 as a part of Ramanujan Fellowship awarded by the Science and Engineering Research Board (SERB), Department of Science and Technology (DST), Government of India. W.K. was supported by the National Research Foundation of Korea (NRF) grant funded by the Korea government (MSIT; NRF-2021R1F1A1061794). The work of M.G.R. is supported by NOIRLab, which is managed by the Association of Universities for Research in Astronomy (AURA) under a cooperative agreement with the National Science Foundation.

Facilities: JCMT (SCUBA2 and POL2).

Software: Starlink (Currie et al. 2014) and Astropy (Astropy Collaboration et al. 2013, 2018).

ORCID iDs

Derek Ward-Thompson https://orcid.org/0000-0003-1140-2761
Janik Karoly https://orcid.org/0000-0001-5996-3600
Kate Pattle https://orcid.org/0000-0002-8557-3582
Anthony Whitworth https://orcid.org/0000-0002-1178-5486
Jason Kirk https://orcid.org/0000-0002-4552-7477
David Berry https://orcid.org/0000-0001-6524-2447
Pierre Bastien https://orcid.org/0000-0002-0794-3859
Tao-Chung Ching https://orcid.org/0000-0001-8516-2532
Simon Coudé https://orcid.org/0000-0002-0859-0805
Jihye Hwang https://orcid.org/0000-0001-7866-2686
Woojin Kwon https://orcid.org/0000-0003-4022-4132
Archana Soam https://orcid.org/0000-0002-6386-2906
Jia-Wei Wang https://orcid.org/0000-0002-6668-974X
Tetsuo Hasegawa https://orcid.org/0000-0003-1853-0184
Shih-Ping Lai https://orcid.org/0000-0001-5522-486X
Keping Qiu https://orcid.org/0000-0002-5093-5088
Doris Arzoumanian https://orcid.org/0000-0002-1959-7201
Tyler L. Bourke https://orcid.org/0000-0001-7491-0048
Do-Young Byun https://orcid.org/0000-0003-1157-4109
Huei-Ru Vivien Chen https://orcid.org/0000-0002-9774-1846
Wen Ping Chen https://orcid.org/0000-0003-0262-272X
Zhiwei Chen https://orcid.org/0000-0003-0849-0692
Jungyeon Cho https://orcid.org/0000-0003-1725-4376
Antonio Chrysostomou https://orcid.org/0000-0002-9583-8644
Eun Jung Chung https://orcid.org/0000-0003-0014-1527
Sophia Dai https://orcid.org/0000-0002-7928-416X
Victor Debattista https://orcid.org/0000-0001-7902-0116
James Di Francesco https://orcid.org/0000-0002-9289-2450
Pham Ngoc Diep https://orcid.org/0000-0002-2808-0888
Yasuo Doi https://orcid.org/0000-0001-8746-6548
Hao-Yuan Duan https://orcid.org/0000-0002-7022-4742
Yan Duan https://orcid.org/0000-0003-3758-7426
Chakali Eswaraiah https://orcid.org/0000-0003-4761-6139
Lapo Fanciullo https://orcid.org/0000-0001-9930-9240
Laura M. Fissel https://orcid.org/0000-0002-4666-609X
Erica Franzmann https://orcid.org/0000-0003-2142-0357
Per Friberg https://orcid.org/0000-0002-8010-8454
Rachel Friesen https://orcid.org/0000-0001-7594-8128
Gary Fuller https://orcid.org/0000-0001-8509-1818
Ray Furuya https://orcid.org/0000-0003-0646-8782
Tim Gledhill https://orcid.org/0000-0002-2859-4600
Sarah Graves https://orcid.org/0000-0001-9361-5781
Jane Greaves https://orcid.org/0000-0002-3133-413X
Qilao Gu https://orcid.org/0000-0002-2826-1902
Saeko Hayashi https://orcid.org/0000-0001-5026-490X
Thiem Hoang https://orcid.org/0000-0003-2017-0982
Martin Houde https://orcid.org/0000-0003-4420-8674
Charles L. H. Hull https://orcid.org/0000-0002-8975-7573
Tsuyoshi Inoue https://orcid.org/0000-0002-7935-8771
Shu-ichiro Inutsuka https://orcid.org/0000-0003-4366-6518
Il-Gyo Jeong https://orcid.org/0000-0002-5492-6832
Doug Johnstone https://orcid.org/0000-0002-6773-459X
Vera Könyves https://orcid.org/0000-0002-3746-1498
Ji-hyun Kang https://orcid.org/0000-0001-7379-6263
Miju Kang https://orcid.org/0000-0002-5016-050X
Akimasa Kataoka https://orcid.org/0000-0003-4562-4119
Koji Kawabata https://orcid.org/0000-0001-6099-9539

Francisca Kemper https://orcid.org/0000-0003-2743-8240
Jongsoo Kim https://orcid.org/0000-0002-1229-0426
Shinyoung Kim https://orcid.org/0000-0001-9333-5608
Gwanjeong Kim https://orcid.org/0000-0003-2011-8172
Kyoung Hee Kim https://orcid.org/0000-0001-9597-7196
Kee-Tae Kim https://orcid.org/0000-0003-2412-7092
Florian Kirchschlager https://orcid.org/0000-0002-3036-0184
Masato I. N. Kobayashi https://orcid.org/0000-0003-3990-1204
Patrick M. Koch https://orcid.org/0000-0003-2777-5861
Takayoshi Kusune https://orcid.org/0000-0002-9218-9319
Jungmi Kwon https://orcid.org/0000-0003-2815-7774
Kevin Lacaille https://orcid.org/0000-0001-9870-5663
Chi-Yan Law https://orcid.org/0000-0003-1964-970X
Chang Won Lee https://orcid.org/0000-0002-3179-6334
Hyeseung Lee https://orcid.org/0000-0003-3465-3213
Yong-Hee Lee https://orcid.org/0000-0001-6047-701X
Chin-Fei Lee https://orcid.org/0000-0002-3024-5864
Jeong-Eun Lee https://orcid.org/0000-0003-3119-2087
Sang-Sung Lee https://orcid.org/0000-0002-6269-594X
Di Li https://orcid.org/0000-0003-3010-7661
Hua-bai Li https://orcid.org/0000-0003-2641-9240
Sheng-Jun Lin https://orcid.org/0000-0002-6868-4483
Hong-Li Liu https://orcid.org/0000-0003-3343-9645
Tie Liu https://orcid.org/0000-0002-5286-2564
Sheng-Yuan Liu https://orcid.org/0000-0003-4603-7119
Junhao Liu https://orcid.org/0000-0002-4774-2998
Steven Longmore https://orcid.org/0000-0001-6353-0170
Xing Lu https://orcid.org/0000-0003-2619-9305
A-Ran Lyo https://orcid.org/0000-0002-9907-8427
Steve Mairs https://orcid.org/0000-0002-6956-0730
Masafumi Matsumura https://orcid.org/0000-0002-6906-0103
Brenda Matthews https://orcid.org/0000-0003-3017-9577
Gerald Moriarty-Schieven https://orcid.org/0000-0002-0393-7822
Tetsuya Nagata https://orcid.org/0000-0001-9264-9015
Fumitaka Nakamura https://orcid.org/0000-0001-5431-2294
Nguyen Bich Ngoc https://orcid.org/0000-0002-5913-5554
Nagayoshi Ohashi https://orcid.org/0000-0003-0998-5064
Takashi Onaka https://orcid.org/0000-0002-8234-6747
Geumsook Park https://orcid.org/0000-0001-8467-3736
Harriet Parsons https://orcid.org/0000-0002-6327-3423
Tae-Soo Pyo https://orcid.org/0000-0002-3273-0804
Lei Qian https://orcid.org/0000-0003-0597-0957
Ramprasad Rao https://orcid.org/0000-0002-1407-7944
Jonathan Rawlings https://orcid.org/0000-0001-5560-1303
Mark Rawlings https://orcid.org/0000-0002-6529-202X
John Richer https://orcid.org/0000-0002-9693-6860
Andrew Rigby https://orcid.org/0000-0002-3351-2200
Giorgio Savini https://orcid.org/0000-0003-4449-9416
Yoshito Shimajiri https://orcid.org/0000-0001-9368-3143
Hiroko Shinnaga https://orcid.org/0000-0001-9407-6775
Mehrnoosh Tahani https://orcid.org/0000-0001-8749-1436
Motohide Tamura https://orcid.org/0000-0002-6510-0681
Ya-Wen Tang https://orcid.org/0000-0002-0675-276X
Xindi Tang https://orcid.org/0000-0002-4154-4309
Kohji Tomisaka https://orcid.org/0000-0003-2726-0892
Le Ngoc Tram https://orcid.org/0000-0002-6488-8227
Serena Viti https://orcid.org/0000-0001-8504-8844
Hongchi Wang https://orcid.org/0000-0003-0746-7968
Jintai Wu https://orcid.org/0000-0001-7276-3590
Jinjin Xie https://orcid.org/0000-0002-2738-146X
Hsi-Wei Yen https://orcid.org/0000-0003-1412-893X
Hyunju Yoo https://orcid.org/0000-0002-8578-1728
Hyeong-Sik Yun https://orcid.org/0000-0001-6842-1555
Yapeng Zhang https://orcid.org/0000-0002-5102-2096
Chuan-Peng Zhang https://orcid.org/0000-0002-4428-3183
Jianjun Zhou https://orcid.org/0000-0003-0356-818X
Philippe André https://orcid.org/0000-0002-3413-2293
David Eden https://orcid.org/0000-0002-5881-3229
Sam Falle https://orcid.org/0000-0002-9829-0426
Valentin J. M. Le Gouellec https://orcid.org/0000-0002-5714-799X
Frédérick Poidevin https://orcid.org/0000-0002-5391-5568
Jean-François Robitaille https://orcid.org/0000-0001-5079-8573
Sven van Loo https://orcid.org/0000-0003-4746-8500

References

Andersson, B. G., Lazarian, A., & Vaillancourt, J. E. 2015, ARA&A, 53, 501
André, P., Di Francesco, J., Ward-Thompson, D., et al. 2014, in Protostars and Planets VI , ed. H. Beuther et al. (Tucson: Univ. Arizona Press), 27
André, P., Men'shchikov, A., Bontemps, S., et al. 2010, A&A, 518, L102
Astropy Collaboration, Price-Whelan, A. M., Sipőcz, B. M., et al. 2018, AJ, 156, 123
Astropy Collaboration, Robitaille, T. P., Tollerud, E. J., et al. 2013, A&A, 558, A33
Barnard, E. E. 1907, ApJ, 25, 218
Benson, P. J., & Myers, P. C. 1989, ApJS, 71, 89
Chandrasekhar, S., & Fermi, E. 1953, ApJ, 118, 116
Chapin, E. L., Berry, D. S., Gibb, A. G., et al. 2013, MNRAS, 430, 2545
Chapman, N. L., Goldsmith, P. F., Pineda, J. L., et al. 2011, ApJ, 741, 21
Chen, C.-Y., King, P. K., & Li, Z.-Y. 2016, ApJ, 829, 84
Crutcher, R. M. 2004, Ap&SS, 292, 225
Currie, M. J., Berry, D. S., Jenness, T., et al. 2014, in ASP Conf. Ser. 485, Starlink Software in 2013, ed. N. Manset & P. Forshay (San Francisco, CA: ASP), 391
Davis, L. 1951, PhRv, 81, 890
Dempsey, J. T., Friberg, P., Jenness, T., et al. 2013, MNRAS, 430, 2534
Doi, Y., Hasegawa, T., Furuya, R. S., et al. 2020, ApJ, 899, 28
Eswaraiah, C., Li, D., Furuya, R. S., et al. 2021, ApJL , 912, L27
Friberg, P., Bastien, P., Berry, D., et al. 2016, Proc. SPIE, 9914, 991403
Guillet, V., Girart, J. M., Maury, A. J., & Alves, F. O. 2020, A&A, 634, L15
Güver, T., & Özel, F. 2009, MNRAS, 400, 2050
Holland, W. S., Bintley, D., Chapin, E. L., et al. 2013, MNRAS, 430, 2513
Howard, A. D. P., Whitworth, A. P., Marsh, K. A., et al. 2019, MNRAS, 489, 962
Johnstone, D., Di Francesco, J., & Kirk, H. 2004, ApJL, 611, L45
Kirchschlager, F., Bertrang, G.-H.-M., & Flock, M. 2019, MNRAS, 488, 1211
Könyves, V., André, P., Men'shchikov, A., et al. 2015, A&A, 584, A91
Kwon, W., Pattle, K., Sadavoy, S., et al. 2022, ApJ, 926, 163
Lee, C. W., Myers, P. C., & Tafalla, M. 2001, ApJS, 136, 703
Lynds, B. T. 1962, ApJS, 7, 1
Lyo, A. R., Kim, J., Sadavoy, S., et al. 2021, ApJ, 918, 85
Mairs, S., Dempsey, J. T., Bell, G. S., et al. 2021, AJ, 162, 191
Marsh, K. A., Kirk, J. M., Andre, P., et al. 2016, MNRAS, 459, 342
Mestel, L. 1965, QJRAS, 6, 265
Naghizadeh-Khouei, J., & Clarke, D. 1993, A&A, 274, 968
Nakano, T., & Nakamura, T. 1978, PASJ, 30, 671
Palmeirim, P., André, P., Kirk, J., et al. 2013, A&A, 550, A38
Pattle, K., Fissel, L., Tahani, M., Liu, T., & Ntormousi, E. 2022a, arXiv:2203.11179
Pattle, K., Lai, S.-P., Di Francesco, J., et al. 2021, ApJ, 907, 88
Pattle, K., Lai, S.-P., Sadavoy, S., et al. 2022b, MNRAS, 515, 1026
Planck Collaboration, Ade, P. A. R., Aghanim, N., et al. 2016, A&A, 586, A138
Punanova, A., Caselli, P., Pineda, J. E., et al. 2018, A&A, 617, A27
Roccatagliata, V., Franciosini, E., Sacco, G. G., Randich, S., & Sicilia-Aguilar, A. 2020, A&A, 638, A85

Schlafly, E. F., Green, G., Finkbeiner, D. P., et al. 2014, ApJ, 786, 29
Seifried, D., Walch, S., Weis, M., et al. 2020, MNRAS, 497, 4196
Seo, Y. M., Majumdar, L., Goldsmith, P. F., et al. 2019, ApJ, 871, 134
Seo, Y. M., Shirley, Y. L., Goldsmith, P., et al. 2015, ApJ, 805, 185
Soler, J. D. 2019, A&A, 629, A96
Soler, J. D., & Hennebelle, P. 2017, A&A, 607, A2
Soler, J. D., Hennebelle, P., Martin, P. G., et al. 2013, ApJ, 774, 128
Torres, R. M., Loinard, L., Mioduszewski, A. J., & Rodriguez, L. F. 2009, ApJ, 698, 242
Wardle, J. F. C., & Kronberg, P. P. 1974, ApJ, 194, 249
Ward-Thompson, D., Pattle, K., Kirk, J. M., et al. 2016, MNRAS, 463, 1008
Ward-Thompson, D., & Whitworth, A. P. 2011, An Introduction to Star Formation (Cambridge: Cambridge Univ. Press)
Yen, H.-W., Koch, P. M., Hull, C. L. H., et al. 2021, ApJ, 907, 33